condensed matter

MDPI

Article

Recent Progress and Perspectives in Positronium Imaging with the $3\gamma/2\gamma$ Ratio

Magdalena Skurzok [1,2]

[1] Faculty of Physics, Astronomy and Applied Computer Science, Jagiellonian University, 30348 Cracow, Poland; magdalena.skurzok@uj.edu.pl
[2] Center for Theranostics, Jagiellonian University, 31501 Cracow, Poland

Abstract

Positronium imaging represents an extension of conventional positron emission tomography, providing information not only about the spatial distribution of the radiopharmaceutical in the human body but also about the molecular environment and tissue architecture. The positronium lifetime and the $3\gamma/2\gamma$ annihilation rate ratio are observables sensitive to the local molecular environment, including the intramolecular free-volume size and oxygen concentration, and may therefore indicate tissue hypoxia. Recent developments in multi-photon detection and event reconstruction have strengthened the feasibility of positronium imaging. Positronium lifetime imaging has already been demonstrated in vivo and is being investigated in clinical and preclinical studies. In contrast, $3\gamma/2\gamma$ ratio imaging remains at the proof-of-concept stage, supported by physical modeling and experimental demonstrations of relative ratio imaging, while quantitative imaging has yet to be validated. This review summarizes recent progress in $3\gamma/2\gamma$ positronium ratio imaging, discusses the main challenges, and outlines its future perspectives and potential applications.

Keywords: positronium; three-photon annihilation; positronium imaging; PET tomography

1. Introduction

Positronium imaging, introduced by Moskal [1], extends conventional positron emission tomography (PET) by enabling the reconstruction of positronium properties using multiphoton detection [2]. One of these properties is the $3\gamma/2\gamma$ decay rate ratio [2,3].

Conventional positron emission tomography (PET) reconstructs the spatial distribution of a positron-emitting radiopharmaceutical from two approximately back-to-back 511-keV photons in coincidence [4,5]. Before annihilation, however, the emitted positron after thermalization in the tissue may form a bound state with an electron known as positronium (Ps). Positronium can be formed in two ground-state spin configurations: para-positronium (pPs) and ortho-positronium (oPs). The pPs singlet state (S = 0) decays predominantly into two photons and has a vacuum mean lifetime of approximately 125ps, while the oPs triplet state (S = 1) undergoes intrinsic three-photon decay with a vacuum mean lifetime of approximately 142ns [6,7].

In condensed biological matter, the properties of oPs are strongly modified by interactions with the surrounding molecular medium [3,6,8–16]. Pick-off annihilation [6] and spin-conversion [17,18] processes strongly shorten its lifetime to the nanosecond range and increase the probability of two-photon annihilation while reducing the contribution of intrinsic three-photon decay. The strength of these effects depends on local tissue properties [3,6]. Larger intramolecular free volumes reduce the interaction of positronium with

Check for updates

Academic Editor: Tullio Scopigno

Received: 29 September 2026
Revised: 5 November 2026
Accepted: 6 November 2026
Published: 11 November 2026

Copyright: © 2026 by the authors. Licensee MDPI, Basel, Switzerland. This article is an open access article distributed under the terms and conditions of the Creative Commons Attribution (CC BY) license.

surrounding electrons, leading to a longer oPs lifetime and an increased probability of 3γ self-annihilation. The presence of oxygen enhances spin conversion processes, shortening the lifetime and increasing the contribution of two-photon annihilation channels relative to three-photon ones. Consequently, both the mean oPs lifetime and the $3\gamma/2\gamma$ annihilation rate ratio can carry information about tissue structure and oxygenation. These observables may potentially enable the assessment of hypoxic conditions, which is crucial for selecting an appropriate cancer therapy [3,19].

These considerations provided the motivation for the development of positronium imaging [1] as an extension of conventional PET, with the positronium lifetime and $3\gamma/2\gamma$ annihilation rate ratio proposed as complementary imaging biomarkers [3,13–15,20]. Currently, promising results toward biomedical applications have been obtained with positronium lifetime imaging (PLI) [2,13,14,21,22]. This method relies on radiopharmaceuticals labeled with positron-emitting radionuclides that additionally emit a prompt gamma photon [23]. The first measurements of the positronium lifetime were carried out by the J-PET group [13,14]. The multiphoton detection capability of the J-PET scanner enables the coincident detection of two annihilation photons and a de-excitation photon, allowing the positronium lifetime to be determined on an event-by-event basis. The developed technique led, in particular, to the first in vivo image of the positronium lifetime distribution in the human brain [14]. These studies were performed using a radiotracer labeled with ^{68}Ga, whose relatively low probability of prompt gamma emission limits the detection efficiency of this approach. Therefore, current efforts are focused on radionuclides with more favorable decay characteristics. Among them, ^{44}Sc is considered a particularly promising candidate for positronium lifetime imaging, as it emits a 1157-keV prompt gamma photon in coincidence with the positron in approximately 94.3% of decays, which may substantially improve the sensitivity of PLI measurements [2,23–26]. Alternative $\beta^+ + \gamma$ emitters, including ^{55}Co and ^{52}Mn, are also being explored for applications involving radiopharmaceuticals with slow pharmacokinetics [27]. At present, positronium lifetime imaging has been demonstrated with only a few PET systems, alongside the development of several dedicated reconstruction methods [2,13,14,21,22,25–35].

The $3\gamma/2\gamma$ annihilation rate ratio provides a complementary observable sensitive to the local molecular environment [3,20,36]. It reflects the relative occurrence of three- and two-photon annihilations, which is influenced by interactions of oPs with the surrounding matter. In contrast to the positronium lifetime imaging, determination of the $3\gamma/2\gamma$ rate ratio does not require detection of additional prompt gamma photons. Consequently, this approach can be implemented using pure positron emitters, including the widely used ^{18}F-FDG radiopharmaceutical [37,38], representing an important practical advantage for potential biomedical applications.

This review summarizes recent developments in positronium imaging based on the $3\gamma/2\gamma$ annihilation rate ratio and discusses its potential as a quantitative biomedical imaging method. The physical principles underlying this approach are presented, followed by an overview of three-photon reconstruction techniques and recent experimental advances. It covers representative theoretical, simulation-based, and experimental studies selected for their relevance to the physical interpretation of the ratio, reconstruction methods, and potential biomedical applications. Particular attention is given to the level of experimental validation, differences in reconstruction assumptions, and limitations of the available approaches. Rather than providing an exhaustive systematic survey, this review critically assesses the progress toward quantitative $3\gamma/2\gamma$ imaging, identifies unresolved methodological challenges, and discusses future perspectives for biomedical and PET applications.

2. Physical Basis of the $3\gamma/2\gamma$ Positronium Imaging

In the biological environment of human tissue, approximately 40% of electron–positron annihilations proceed through the formation of an intermediate positronium state [3,10,15]. The remaining 60% corresponds to direct e^+e^- annihilation. These two possible annihilation pathways with fractions f_{Ps} and f_{d} are illustrated in Figure 1 and are represented by the blue and orange branches, respectively [3]. The figure also shows the possible annihilation processes of pPs and oPs, formed with fractions f_{pPs} and f_{oPs}, respectively, together with their corresponding rates (λ) and probabilities (α, β).

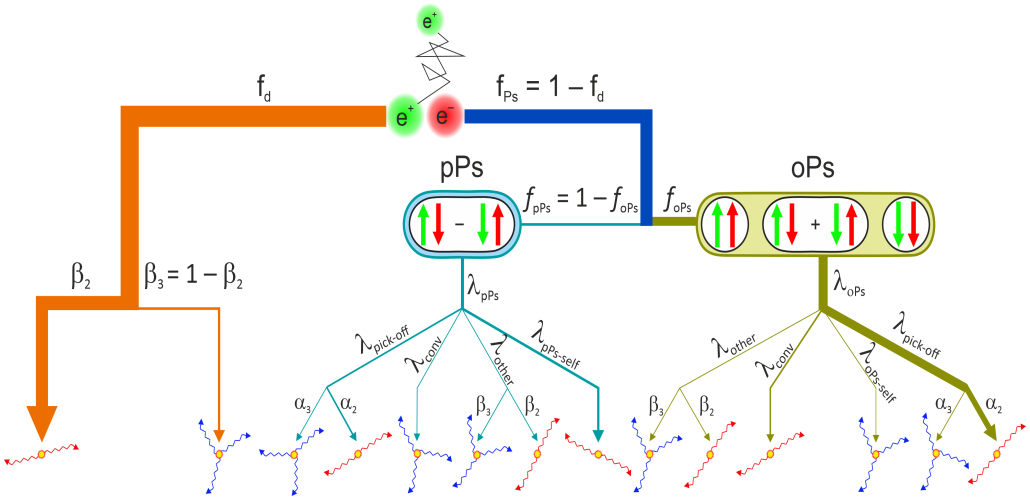


Figure 1. Schematic representation of the possible two- and three-photon e^+e^- annihilation processes in tissue. Here, f_{d} and f_{Ps} indicate fractions of direct annihilation and annihilation via positronium formation. In biological tissues, the ratio $f_{\mathrm{d}}/f_{\mathrm{Ps}}$ can vary substantially with tissue properties from about 3/2 to 1/4, and f_{pPs} and f_{oPs} are relative fractions of pPs and oPs formation, respectively. λs denote decay rates of possible annihilation processes, while αs and βs represent intrinsic branching fractions of 2γ and 3γ emission. Details regarding processes shown in this figure are available in the text. This scheme is adopted from [3].

The direct e^+e^- annihilation results in the emission of two or three photons, with a $3\gamma/2\gamma$ probability ratio β_3/β_2 of 1:372 (as follows from LO calculations [39]). Positronium formed in biological materials can occur in either the ortho- or para-spin state, with the ratio $f_{\mathrm{oPs}}/f_{\mathrm{pPs}}$ potentially deviating from three, as expected from the spin statistics [3]. It can undergo annihilation not only through its intrinsic decay channels but also through interactions with the surrounding molecular environment. The total Ps decay rate in the biological medium can therefore be expressed as follows:

$$\lambda_{\mathrm{Ps}} = \lambda_{\mathrm{Ps\text{-}self}} + \lambda_{\mathrm{pick\text{-}off}} + \lambda_{\mathrm{conv}} + \lambda_{\mathrm{other}}, \quad (1)$$

where $\lambda_{\mathrm{Ps\text{-}self}}$ denotes the intrinsic self-annihilation rate (pPs $\rightarrow 2\gamma$ or oPs $\rightarrow 3\gamma$), while $\lambda_{\mathrm{pick\text{-}off}}$, λ_{conv}, and λ_{other} represent pick-off annihilation, spin conversion, and other chemical quenching processes, respectively. The inverse of the decay rate determines the positronium lifetime, i.e., $\tau_{\mathrm{pPs}} = 1/\lambda_{\mathrm{pPs}}$ and $\tau_{\mathrm{oPs}} = 1/\lambda_{\mathrm{oPs}}$. The self-annihilation rates (in a vacuum) for pPs and oPs are $\lambda_{\mathrm{pPs\text{-}self}} = 7990.9\ \mu\mathrm{s}^{-1}$ and $\lambda_{\mathrm{oPs\text{-}self}} = 7.04\ \mu\mathrm{s}^{-1}$, respectively, as determined from measurements reported in [40,41] and found to be consistent with QED theory [42]. The corresponding lifetimes of para- and ortho-positronium are 125ps and 142ns, respectively. The remaining processes occur with decay rates to the order of $500\ \mu\mathrm{s}^{-1}$, resulting in a significant effect on the oPs lifetime, while their impact on the pPs lifetime is comparatively small. This makes oPs particularly sensitive to changes in the tissue environment, highlighting its potential as a biomarker of tissue pathology [3,19].

The pick-off process occurs when the positron bound in positronium annihilates with an electron from the surrounding molecules, resulting predominantly in the emission of two photons (the relative contribution of 3γ to 2γ pick-off annihilations is $\alpha_3/\alpha_2 \sim 1/378$ [6]). The pick-off annihilation rate $\lambda_{\text{pick-off}}$ depends on the properties of the surrounding material, particularly the size of the free voids available for positronium. And for a good approximation, it can be considered independent of the positronium spin state, i.e., $\lambda^{\text{pPs}}_{\text{pick-off}} = \lambda^{\text{oPs}}_{\text{pick-off}}$ [6]. The dependence of the oPs lifetime on the size of the free volume is commonly described by the Tao–Eldrup model [43,44]. The experimentally determined values of $\lambda_{\text{pick-off}}$ for water and adipose tissue are 513–550 μs^{-1} [17,18] and 368 μs^{-1} [3], respectively.

Positronium formed in matter can also interact chemically with its surrounding environment, particularly radiolytic products such as hydrated electrons, hydronium ions (H_3O^+), and hydroxyl radicals generated during positron thermalization, as well as with other dissolved substances, including molecular oxygen [6,18]. The interaction of positronium with dissolved paramagnetic molecules, such as O_2, can induce spin conversion processes through interactions with their unpaired electrons. As a result, oPs can be converted into pPs, which subsequently undergoes rapid self-annihilation into two photons (oPs + O_2 $\rightarrow$ pPs + O_2 $\rightarrow$ $2\gamma + O_2$). Conversely, pPs can also undergo spin conversion into oPs, which subsequently decays predominantly into three photons (pPs + O_2 $\rightarrow$ oPs + O_2 $\rightarrow$ $3\gamma + O_2$).

The main "other" chemical quenching process associated with interactions with molecular oxygen is oxidation. In this process, Ps interacts with O_2, leading to electron transfer and the formation of an oxygen ion and a free positron ($\text{Ps} + O_2 \rightarrow e^+ + O_2^-$). The released positron subsequently undergoes direct annihilation with an electron from the surrounding medium, resulting in the emission of two or three photons whose ratio is assumed to be the same as in case of direct annihilation (β_3/β_2) [3].

For oxygen dissolved in tissue, the ratio of the rate of "other" processes involving positronium–oxygen interactions, predominantly oxidation, to the spin conversion rate $\lambda_{O_2\text{-other}}/\lambda_{O_2\text{-conv}}$ ranges from 0.1 to 0.2, as shown in [3,17,18]. The rate λ_{O_2} corresponding to positronium interactions with dissolved oxygen, including conversion and oxidation, increases linearly with oxygen pressure and, consequently, with the concentration of dissolved oxygen molecules [3]. For the investigated mimicking substances (water, adipose tissue, isopropanol, cyclohexane, and isooctane), λ_{O_2} ranges from 0 to 40 μs^{-1} over the oxygen pressure range of 0–60 mmHg, which is relevant for biological tissues [3,6,19]. The largest effect associated with oxygen-induced interactions is observed for isooctane, while for adipose tissue, the corresponding rate is approximately four times lower at the same oxygen pressure. In water, by contrast, the rate is 27 μs^{-1} [6] at an oxygen concentration of 1400 $\mu molL^{-1}$, which is approximately 40% lower than that observed for adipose tissue under the corresponding condition. These observations indicate that positronium may provide a means of assessing the oxygen concentration and, potentially, the oxygen partial pressure in biological tissues, making positronium-based measurements particularly promising for the noninvasive assessment of tissue hypoxia [3].

Considering the different mechanisms contributing to two- and three-photon annihilation (shown in Figure 1), and assuming that molecular oxygen is the only dissolved gas, the authors of [3] derived the expression for the $3\gamma/2\gamma$ annihilation rate ratio $R_{3\gamma/2\gamma}$ for one void type (Equation (6) in [3]). The annihilation rate ratio depends on several properties of the medium and positronium formation. In particular, it is determined by (i) the size of the free-volume regions between molecules, which affects the pick-off annihilation rate ($\lambda_{\text{pick-off}}$); (ii) the concentration of paramagnetic O_2, which influences the rates of spin conversion and other positronium–oxygen interactions ($\lambda_{O_2\text{-conv}}$ and $\lambda_{O_2\text{-other}}$); (iii) the

density of free-volume regions, reflected in the positronium formation fraction (f_{Ps}); and (iv) the relative formation probabilities of para- and ortho-positronium ($f_{\mathrm{pPs}}/f_{\mathrm{oPs}}$). Since oPs is considerably more sensitive to the surrounding medium than pPs, the ratio derived in [3] reads as

$$R_{\mathrm{oPs}-3\gamma/2\gamma} = \frac{\lambda_{o\mathrm{Ps}\text{-}self} + \alpha_3\lambda_{\text{pick-off}} + \beta_3\lambda_{\mathrm{O_2\text{-other}}}}{\alpha_2\lambda_{\text{pick-off}} + \beta_2\lambda_{\mathrm{O_2\text{-other}}} + \lambda_{\mathrm{O_2\text{-conv}}}} \tag{2}$$

for the oPs annihilation rate with three photons compared with that for two photons. Unlike $R_{3\gamma/2\gamma}$ (see Equation (6) in [3]), the oPs-specific ratio $R_{\mathrm{oPs}-3\gamma/2\gamma}$ does not explicitly depend on the positronium formation fraction or the relative pPs/oPs formation ratio, making it potentially more sensitive to oxygen-dependent processes [3]. This independence arises since the oPs formation probability cancels when considering the ratio of the competing three- and two-photon annihilation channels, assuming the processes described by Equation (2). While the total ratio can be experimentally determined from corrected 2γ and 3γ event counts, the oPs-specific ratio directly reflects the annihilation processes originating from oPs. Its determination can be achieved by identifying oPs-related annihilation contributions or by applying a physical model accounting for the different annihilation channels [3].

An alternative, simplified formulation of the total $R_{3\gamma/2\gamma}$ ratio uses positronium lifetimes and intensities obtained from PALS measurements [10,36]. In this approach, the absolute fraction $f_{3\gamma}$ of three-photon annihilations is expressed as the sum of the contribution from direct positron–electron annihilation and that from oPs self-annihilation:

$$f_{3\gamma} = f_{3\gamma\text{-direct}} + f_{3\gamma\text{-oPs}}. \tag{3}$$

Assuming a statistical, unpolarized positronium formation ($f_{\mathrm{oPs}} = 3/4$, $f_{\mathrm{pPs}} = 1/4$), and identifying the measured oPs intensity with its formation probability $I_{\mathrm{oPs}} = f_{\mathrm{Ps}}f_{\mathrm{oPs}}$, the direct annihilation fraction becomes $f_{\mathrm{d}} = 1 - \frac{4}{3}I_{\mathrm{oPs}}$. For a direct three-to-two-photon branching ratio $\beta_3/\beta_2 = 1/372$, the normalized three-photon branching fraction is $\beta_3 = 1/373$. The total three-photon fraction is then approximated by

$$f_{3\gamma} \simeq \beta_3\left(1 - \frac{4}{3}I_{\mathrm{oPs}}\right) + I_{\mathrm{oPs}}\frac{\tau_{\mathrm{oPs}}}{\tau_{\mathrm{oPs-self}}}, \tag{4}$$

where τ_{oPs} is the measured oPs lifetime and $\tau_{oPs-\mathrm{self}}$ is its intrinsic lifetime in vacuum. The corresponding ratio is

$$R_{3\gamma/2\gamma} = \frac{f_{3\gamma}}{1 - f_{3\gamma}}. \tag{5}$$

This PALS-based formulation provides an experimentally accessible estimate of the total $R_{3\gamma/2\gamma}$ ratio from the measured oPs lifetime and intensity [36], assuming statistical pPs/oPs formation and that the measured PALS intensity reflects the initial oPs formation probability. Deviations from these assumptions or additional annihilation processes may affect the inferred ratio. Unlike the oPs-specific quantity $R_{\mathrm{oPs}-3\gamma/2\gamma}$, the total ratio depends on the positronium formation fraction and the relative populations of both spin states. Therefore, the two ratios provide complementary information on positronium formation and its interactions with the surrounding medium [10,36].

3. Advances in Three-Photon Reconstruction and $3\gamma/2\gamma$ Imaging

The determination of the spatially resolved $3\gamma/2\gamma$ annihilation rate ratio requires two independent reconstructions: one for two-photon annihilation events and another for three-photon events. The reconstruction of 2γ events is well established in conventional PET. In this case, positron-electron annihilation produces two approximately back-to-back photons

with energies close to 511 keV, and their coincident detection defines a line of response (LOR) along which the annihilation point is located. Standard PET reconstruction algorithms can then be used to recover the spatial distribution of two-photon annihilations [25,45].

Reconstructing oPs $\rightarrow 3\gamma$ events is more challenging because three-photon annihilation involves a more complex kinematic phase space than the two-photon process. In 3γ decay, the available annihilation energy is continuously shared among the three photons with the total energy conserved, while their emission directions are constrained by momentum conservation [46,47]. As a consequence, one cannot define a conventional line of response (LOR), and dedicated reconstruction methods are required to localize the annihilation point event by event [48]. The three-photon annihilation position reconstruction methods have recently been developed based on the complementary information provided by the detected photons, including their interaction positions, detection times, and deposited energies. Two main strategies can be distinguished: (1) based on the measured interaction positions and detection times of the three photons and (2) combining interaction positions with photon energies applying the kinematic constraints.

The first method developed by the J-PET group applies a trilateration-based reconstruction approach [49] (Figure 2). In this method, the annihilation point is reconstructed as the common intersection of three circles defined within the decay plane from the measured photon interaction positions $\mathbf{r_i}$ and detection times t_i ($i = 1, 2, 3$). For each photon, the corresponding circle is centered at $\mathbf{r}_i$, while its radius is given by the distance traveled by the photon from the annihilation point to the detector, $c(t_i - t_a)$. The annihilation position $\mathbf{r}$ therefore satisfies $|\mathbf{r}_i - \mathbf{r}| = c(t_i - t_a)$, where t_a denotes the annihilation time. The common intersection of the three constraints determines both the reconstructed 3γ annihilation position and the corresponding annihilation time (Figure 2b). The method, initially developed and validated using Monte Carlo simulations [49], was subsequently applied to experimental data acquired with the J-PET detector (see Figure 2a), a multi-photon detection system based on plastic scintillator strips [14]. Using this approach, annihilation points were reconstructed in extended cylindrical (Figure 2c) and spherical positronium production chambers with a spatial resolution of approximately 8 cm [48,50]. These studies confirmed the feasibility of three-photon imaging based on the measured spatial and timing information.

A complementary 3γ reconstruction strategy uses the measured energies and interaction positions of the three annihilation photons. For an annihilation at rest, energy and momentum conservation require the sum of photon energies to equal the total energy released in the annihilation ($E_1 + E_2 + E_3 = 2m_e c^2$), while the three photon momenta lie in a common plane. The opening angles θ_{ij} between the coplanar photons i and j are determined by their energies according to $\theta_{ij} = \arccos\left(\frac{-E_i^2 - E_j^2 + E_k^2}{2E_i E_j}\right)$. Consequently, combining the measured energies and interaction positions of the three photons provides the geometrical and kinematic constraints required for event-by-event reconstruction of the annihilation point. This principle was first experimentally investigated by Abuelhia et al. [51] using three high-resolution detectors in triple coincidence and advanced by Fujimoto et al. [36] (Figure 3). A simplified analytical reconstruction method suitable for a PET-like detector geometry was introduced. In the reconstruction procedure, the three-photon decay plane is mapped onto a two-dimensional complex plane, in which the measured photon energies determine the corresponding opening angles. Two circles are then constructed: C_1 and C_2, defined by the interaction positions P_1, P_2 and angle θ_{12} and by P_2, P_3, and θ_{23}, respectively (see Figure 3b). The annihilation point Q is identified as the intersection of the two circles, excluding the common intersection at the known detector position P_2. This geometrical formulation reduces the localization problem to solving a set of quadratic equations and

enables direct event-by-event reconstruction of the 3γ annihilation (see Figure 3c) position without requiring time-of-flight information.

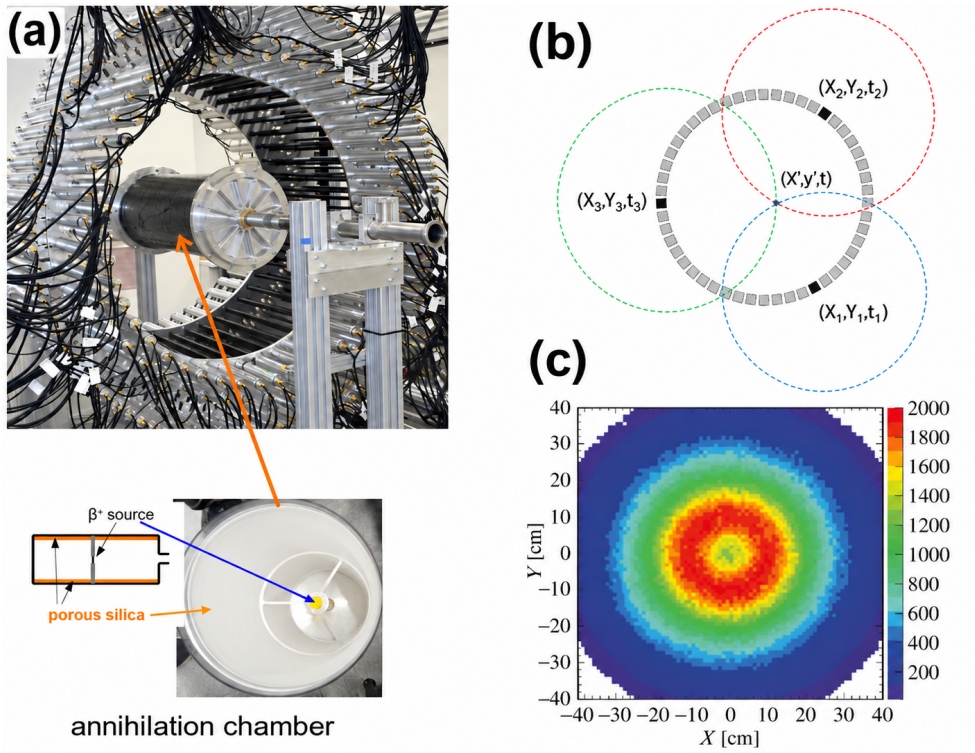


Figure 2. Methodology of the 3γ annihilation reconstruction with the J-PET. (**a**) Photograph of the J-PET tomograph system with the annihilation chamber. The tomograph consists of 192 plastic scintillators (black strips) read on both sides by photomultipliers (silver pipes), arranged into three concentric cylinders, which detect photons produced in oPs$\rightarrow 3\gamma$ reaction. The positronium annihilation chamber contains a sodium source in the center and a cylindrical wall coated with porous silica for effective production of positronium atoms. (**b**) Trilateration method scheme shown in two-dimentional plane. For each photon, the hit position defines a circle of possible decay points, with its radius determined by the detection time and the unknown oPs annihilation time. The annihilation point is obtained from the intersection of the three circles as described in text. (**c**) Reconstructed spatial distribution of the identified oPs$\rightarrow 3\gamma$ events obtained using three-photon annihilations, allowing us to reproduce a tomographic image of the vacuum chamber. Figures are adopted from [48].

With this reconstruction approach, 3γ imaging was performed, and for the first time, $3\gamma/2\gamma$ experimental ratio was demonstrated using a ring-shaped detector system composed of eight modules based on pixelated high-energy resolution HR-GAGG scintillators [36] (see Figure 3a). The ratio was determined by combining directly reconstructed 3γ distribution with a conventional 2γ PET image. The relative enhancement of the $3\gamma/2\gamma$ ratio in the XAD-4 porous material with respect to water was measured to be 1.77 ± 0.09, in good agreement with the theoretical value 1.78 ± 0.24 derived from PALS data [52,53]. The reported images represent relative rather than absolute $3\gamma/2\gamma$ ratios, since an absolute ratio would additionally require corrections for the different detection efficiencies of the two annihilation channels. Moreover, quantitative $3\gamma/2\gamma$ imaging involves further challenges related to random coincidences, photon attenuation, and scattered events, which require dedicated correction procedures and are discussed in Section 4. Table 1 summarizes the presented studies on 3γ reconstruction and $3\gamma/2\gamma$ ratio imaging, highlighting the methods, validation approaches, and main achievements and limitations.

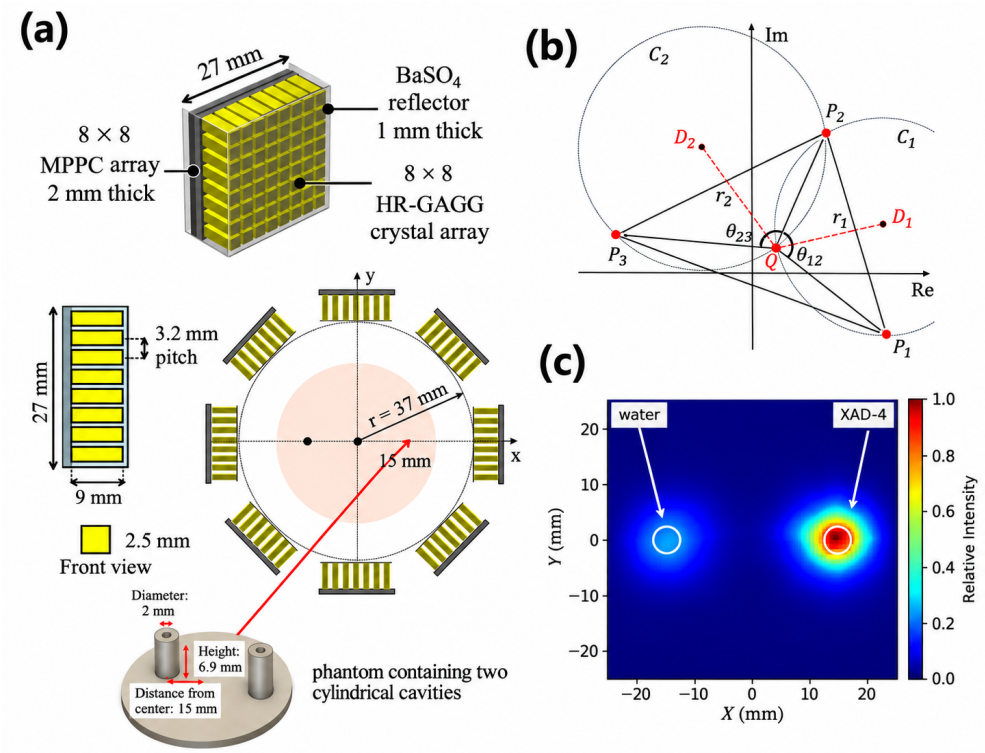


Figure 3. Methodology of the 3γ annihilation reconstruction by Fujimoto et al. [36] (**a**) Schematic of the detector ring geometry and used phantom. The detector consists of eight detector modules arranged in a circular configuration with a radius of 37 mm. Each module consists of an 8 × 8 HR-GAGG scintillator array separated by BaSO4 reflectors and coupled to an 8 × 8 MPPC array. The 3D-printed phantom containing two cylindrical cavities was positioned 15 mm from the center (one cavity contained water, while the second contained XAD-4 porous material). (**b**) Scheme of energy-based three-photon imaging method. The annihilation position Q is mathematically determined as the intersection of two circles, C1 and C2, in the complex plane as described in text. (**c**) The image is of reconstructed 3γ annihilation points. Figures are adopted from [36].

Table 1. Studies relevant to three-photon reconstruction and 3γ/2γ ratio imaging.

Detector or MC Simulations	Reconstruction Approach	Sample/Validation	Performance/Correction Methods	Ratio Imaging/Main Limitations
J-PET [49]	Time-based trilateration	Monte Carlo simulated oPs $\rightarrow$ 3γ events (GEANT 4)	Reconstruction feasibility/no	No/simulation-based study
J-PET [48]	Three-photon event reconstruction, time-based trilateration	Experimental data, positronium-production chamber	Reconstructed oPs $\rightarrow$ 3γ spatial distribution/no	No/study focused on symmetry observables
MC simulations [46]	Simulation of 2γ and 3γ photon transport (GATE)	Phantom models (simple and XCAT human phantom)	Energy- and geometry-dependent attenuation analysis/no	No/simulation support for future corrections
Three-detector system [51]	Energy- and geometry-based 3γ localization	Experimental data, 2D three-photon imaging	Demonstration of source localization in restricted geometry/no	No/limited detector geometry
HR-GAGG ring [36]	Energy-based 3γ reconstruction	Experimental data, Water/XAD-4 phantom/comparison with PALS prediction	Relative XAD-4/water ratio 1.77 $\pm$ 0.09; PALS-based reference 1.78 $\pm$ 0.24/no	Relative ratio imaged/absolute quantitative accuracy not established

4. Toward Quantitative $3\gamma/2\gamma$ Imaging — Challenges

Reliable quantitative $3\gamma/2\gamma$ imaging requires appropriate event reconstruction criteria for both 2γ and 3γ channels together, with dedicated corrections for the physical and instrumental effects that affect the two types of annihilation events differently.

A major challenge is the different identification and reconstruction of 2γ and 3γ events. While conventional PET uses coincident 511-keV photon pairs to define lines of response, 3γ imaging requires triple-coincidence detection and dedicated reconstruction methods based on photon interaction positions, energies, or detection times (see Section 3). The event selection and reconstruction procedures for 3γ imaging are still under development and require further optimization [36,48].

A further challenge is related to dedicated corrections that account for the different effects of photon attenuation, detector response, geometrical acceptance, scatter, and random coincidences in the 2γ and 3γ events. For a given annihilation channel c ($c = 2\gamma$ or 3γ), the measured number of reconstructed events assigned to voxel r = (i,j,k) can be presented in the following form:

$$N_c^{\mathrm{exp}}(\mathbf{r}) = \epsilon_c(\mathbf{r}) A_c(\mathbf{r}) N_c^{\mathrm{corr}}(\mathbf{r}) + S_c(\mathbf{r}) + R_c(\mathbf{r}), \tag{6}$$

where N_c^{corr} represents the corresponding number of physical annihilations before detection losses and background contributions. The factor ϵ_c includes detector acceptance, event selection and reconstruction efficiency, and $A_c(r)$ represents the probability that the annihilation photons reach the detector without attenuation. The terms $S_c(\mathbf{r})$ and $R_c(\mathbf{r})$ describe the contributions from scattered photons and random coincidences, respectively. The corrected voxel-wise $3\gamma/2\gamma$ ratio can then be estimated as follows:

$$R_{3\gamma/2\gamma}^{\mathrm{corr}}(\mathbf{r}) = \frac{N_{3\gamma}^{\mathrm{exp}}(\mathbf{r}) - S_{3\gamma}(\mathbf{r}) - R_{3\gamma}(\mathbf{r})}{N_{2\gamma}^{\mathrm{exp}}(\mathbf{r}) - S_{2\gamma}(\mathbf{r}) - R_{2\gamma}(\mathbf{r})} \frac{\epsilon_{2\gamma}(\mathbf{r}) A_{2\gamma}(\mathbf{r})}{\epsilon_{3\gamma}(\mathbf{r}) A_{3\gamma}(\mathbf{r})}. \tag{7}$$

In practice, the efficiency can be evaluated using Monte Carlo simulations incorporating detector geometry, response, and event selection criteria [54,55]. Photon attenuation corrections can be derived from attenuation maps, typically obtained from CT data, accounting for the photon energies and trajectories [45,46,56,57]. Scatter contributions can be estimated using Monte Carlo [45,58] or model-based simulations [59,60], while random coincidences can be evaluated from delayed-coincidence measurements or statistical models of the coincidence rates [45,61,62]. These corrections must be determined separately for the 2γ and 3γ channels due to their different photon multiplicities, energy distributions, and detection efficiencies.

The corrected voxel-wise ratio, $R_{3\gamma/2\gamma}^{\mathrm{corr}}(\mathbf{r})$, provides an estimate of the local physical $3\gamma/2\gamma$ annihilation rate ratio. Its quantitative accuracy depends on the applied corrections and the assumptions of the reconstruction model.

Although corrections for attenuation, scatter, and random coincidences are well established in conventional 2γ PET [45,58], their application to 3γ imaging requires dedicated models accounting for differences in photon multiplicity, energy distribution, and detection characteristics.

Photon attenuation is one of the effects that differs fundamentally between the 2γ and 3γ annihilation channels. In conventional PET, the two annihilation photons have energies of approximately 511 keV and propagate in nearly opposite directions. Their attenuation can therefore be described using a single energy attenuation map, typically derived from CT data, and evaluated along the corresponding line of response (LOR) [45,56,57]. The situation is more complex for oPs $\rightarrow 3\gamma$ events. The three photons share the total annihilation energy of 1022 keV, and their individual energies are continuously distributed below 511 keV. In

addition, the three photons propagate along different trajectories through the object. The probability that a complete 3γ event escapes the tissue without interaction depends on the energy and path of each photon as well as on the object composition, and it is a few times lower than in the case of the 2γ channel [46]. Attenuation maps for the 3γ channel should be therefore determined while taking into account the kinematics of the $oPs \rightarrow 3\gamma$ process [47], as well as the object composition and geometry.

Scattered and random coincidences represent additional sources of bias that must be corrected in quantitative $3\gamma/2\gamma$ imaging. In conventional 2γ PET, scattered coincidences arise when one or both 511-keV annihilation photons undergo Compton scattering in the patient or phantom before detection, resulting in an incorrect assignment of the corresponding LOR. Scatter is estimated using model-based approaches such as Single scatter simulation (SSS) [59,60] or Monte Carlo [45,58] methods, which use the activity distribution together with the attenuation map to model photon transport and scattering within the object [45,58]. The estimated scatter contribution is then incorporated into the iterative image reconstruction procedure. Random coincidences in PET originate from photons belonging to independent annihilations that are detected within the same coincidence time window. Their contribution can be estimated, for example, using delayed-coincidence windows [45,61,62] and included as an additive background term during the reconstruction. Scatter and random corrections are more complex for 3γ imaging. The three-body topology of the 3γ annihilation, characterized by three coplanar photons with continuously distributed energies [47], requires dedicated scatter models that simultaneously account for photon transport and attenuation. In turn, random-coincidence correction should account for the different combinations of unrelated photons that can satisfy the triple-coincidence condition, including a true 2γ event accompanied by an unrelated third photon, as well as three photons originating from independent 3γ annihilation events.

An additional challenge for $3\gamma/2\gamma$ imaging is the limited detection sensitivity of three-photon events, requiring triple-coincidence registration and sufficient counting statistics. Detector energy resolution and event selection criteria also affect the accuracy of the reconstructed ratio. In patient-sized objects, photon attenuation, scattering, and random triple coincidences further limit sensitivity and may increase acquisition times. Therefore, dedicated simulations and experimental validation are needed to evaluate the feasibility and quantitative performance of $3\gamma/2\gamma$ imaging under clinically relevant conditions.

Even after instrumental and physical corrections are introduced, quantitative interpretation of the reconstructed $3\gamma/2\gamma$ ratio remains challenging, as it depends on several properties of the local medium, including free-volume size, positronium formation probability, and oxygen concentration. Therefore, variations in the measured ratio cannot be directly attributed to a single biological parameter, such as oxygen concentration, since changes in tissue morphology may produce similar effects (see Section 5). Moreover, it is important to distinguish between the feasibility of reconstructing $3\gamma/2\gamma$ ratio images and the quantitative accuracy of the reconstructed physical ratio. Initial J-PET studies demonstrated the feasibility of three-photon reconstruction using Monte Carlo simulations and experimental data acquired with positronium production chambers [48,49]. The relative $3\gamma/2\gamma$ ratio imaging demonstrated by Fujimoto et al. [36] provides an important experimental proof of concept (see Section 3) but does not yet establish absolute quantitative accuracy that requires appropriate corrections for detection efficiency, attenuation, scatter, and random coincidences, as well as systematic validation using reference materials and tissue-like phantoms with well-characterized properties. Therefore, quantitative $3\gamma/2\gamma$ ratio imaging in biological tissues and in vivo remains an important aim for future studies.

5. Biomedical Relevance of Positronium-Sensitive Observables

The sensitivity of the positronium lifetime and the $3\gamma/2\gamma$ annihilation rate ratio to the local molecular environment provides the basis for their potential biomedical applications [3,6]. Unlike conventional PET, which primarily reflects radiopharmaceutical uptake, positronium-sensitive observables may provide complementary information on tissue microstructure and oxygenation. Their dependence on molecular free volume and oxygen-induced interactions is discussed in Section 2.

5.1. Tissue Structure

One of the most important environmental parameters affecting oPs is the free volumes available within the surrounding molecular structure and their concentration [6,8,9,11]. The oPs formation probability depends on the void density, whereas the oPs lifetime is strongly influenced by the overlap between the positronium wave function and electrons belonging to neighboring molecules. In larger molecular voids, this overlap is reduced, resulting in a lower probability of pick-off annihilation [6]. Consequently, oPs can survive for a longer time, and a larger fraction of oPs atoms may undergo intrinsic three-photon self-annihilation, thereby leading to a higher $R_{3\gamma/2\gamma}$ ratio [3,10]. In turn, in smaller free-volume voids, pick-off annihilation becomes more probable, leading to a shorter oPs lifetime and an increased contribution of the two-photon annihilation channel.

Therefore, changes in tissue structure, including molecular packing, hydration level, and lipid composition, which are related to the organization of free-volume voids, can significantly affect positronium's properties. It has been shown that in biological membranes, the oPs lifetime varies with the cholesterol and phospholipid content [63], which influence molecular packing, membrane fluidity, and its local nanostructure. Changes in the degree of hydration and dehydration processes also modify the free-volume fraction, which is reflected in pronounced changes in the mean oPs lifetime and its intensity [64–66]. This shows that the determination of positronium-sensitive observables is a highly promising approach for investigating tissue nanostructure and morphology.

5.2. Oxygenation and Hypoxia

Molecular oxygen dissolved in the tissue represents another important environmental factor affecting positronium annihilation, predominantly through spin conversion and oxidation processes [3,17]. An increase in the oxygen concentration is therefore expected to enhance the relative contribution of the two-photon annihilation channels and shorten the mean oPs lifetime. By contrast, reduction in the oxygen concentration may prolong the oPs lifetime and increase the $3\gamma/2\gamma$ annihilation rate ratio [3].

This dependence is of particular biomedical interest for assessing the degree of hypoxia, characterized by reduced tissue oxygenation, which is a common feature of many solid tumors and associated with tumor progression, metastasis, and resistance to various forms of therapy [3,67–69]. Recent theoretical investigations have predicted the dependence of τ_{oPs} and $R_{3\gamma/2\gamma}$ on the oxygen concentration and partial pressure in water, several organic liquids (isooctane, isopropanol, and cyclohexane), and adipose tissue [3]. These materials provide useful reference systems, since water is the major constituent of biological cells, while organic media can mimic selected lipid-rich and hydrophobic environments as well as certain cellular metabolites. The study showed, among other findings, that distinguishing physoxic conditions (corresponding to partial oxygen pressure of $p_{O_2} = 50$ mmHg in healthy tissue [70]) from hypoxic conditions (corresponding to $p_{O_2} = 10$ mmHg [68]) in adipose tissue would require measurement precisions several times better than 48ps for τ_{oPs} and 4×10^{-4} for $R_{\mathrm{oPs}-3\gamma/2\gamma}$. It was also shown that the change of $R_{\mathrm{oPs}-3\gamma/2\gamma}$ with oxygen pressure was significantly larger than that observed for $R_{3\gamma/2\gamma}$, as discussed in Section 2,

and that variations in the oxygen concentration modified the relative contributions of pick-off annihilation, direct annihilation, and spin conversion processes.

Although τ_{oPs} and $R_{oPs-3\gamma/2\gamma}$, considered individually, are sensitive to tissue oxygenation, neither parameter appears to be sufficient for a robust assessment of oxygenation and hypoxia [3]. Both observables are influenced not only by the oxygen concentration but also by the structural properties of the local tissue. In particular, tissue heterogeneity, variations in the molecular free volume, and differences in tissue composition can significantly modify the pick-off annihilation rate and, consequently, the measured values of τ_{oPs} and $R_{oPs\text{-}3\gamma/2\gamma}$ [3]. Experimental studies have shown that patient-to-patient and tissue-to-tissue variations in τ_{oPs} may be larger than the changes expected solely from the difference in oxygen concentration between physoxic and hypoxic conditions [19]. Therefore, relying on either τ_{oPs} or $R_{oPs-3\gamma/2\gamma}$ alone may make it difficult to distinguish effects arising from tissue microstructure and oxygenation.

The simultaneous determination of τ_{oPs} and $R_{oPs-3\gamma/2\gamma}$ may provide complementary information on oxygen-dependent annihilation processes and tissue microstructure [3]. Since these observables respond differently to pick-off annihilation and oxygen-induced interactions, their simultaneous analysis may help distinguish structural and oxygen-related effects. This motivates the development of multiparametric positronium imaging combining conventional PET activity, the oPs lifetime, formation probability, and the $3\gamma/2\gamma$ ratio.

6. Conclusion and Perspectives

Positronium imaging based on the $3\gamma/2\gamma$ annihilation rate ratio is a promising extension of conventional PET. It could provide information about the local molecular environment in addition to the spatial distribution of a radiopharmaceutical. Moreover, determination of the $3\gamma/2\gamma$ ratio does not require the detection of an additional prompt gamma photon, like in the case of positronium lifetime imaging, and can therefore be performed with pure positron emitters, including widely used ^{18}F-based radiotracers. Recent advances in multiphoton detection [13,14,36,48] and the development of the dedicated three-photon event reconstruction methods [36,48] have shown the experimental feasibility of 3γ imaging and enabled the first relative $3\gamma/2\gamma$ ratio image.

The quantitative $3\gamma/2\gamma$ imaging remains, however, a major challenge. It requires a proper framework accounting for 2γ and 3γ event reconstruction procedures, detector effects, photon attenuation, scatter, and random coincidences. Independent event selection criteria for 2γ and 3γ annihilation channels should be developed together with dedicated corrections of attenuation and scattered and random coincidences for each channel. In particular, dedicated attenuation and scatter models accounting for the continuous energy distribution and three-photon topology of 3γ annihilation are required, together with reliable estimates of random triple coincidences and determination of the 2γ and 3γ detection efficiencies.

From the biomedical perspective, the $3\gamma/2\gamma$ ratio is sensitive to several properties of the tissue environment, including the molecular free volume and oxygen concentration. It therefore represents a promising tool for investigating tissue microstructure and oxygenation. Together with the complementary positronium observable, the oPs lifetime, it may help distinguish structural effects from those related to tissue oxygenation and provide a more comprehensive characterization of the local tissue environment. Combining conventional PET activity imaging with the oPs lifetime and $3\gamma/2\gamma$ ratio measurements may enable multiparametric imaging for a more comprehensive characterization of tissue microstructure and oxygenation in vivo.

Funding: This research was supported by the National Science Centre of Poland through grants MAESTRO no. 2021/42/A/ST2/00423; OPUS no. 2021/43/B/ST2/02150; and OPUS24+LAP no. 2022/47/I/NZ7/03112; the Ministry of Science and Higher Education through grant no. IAL/SP/596235/2023 and SPUB/SP/627733/2025; the European Union within the Horizon Europe Framework Programme through ERC Advanced Grant POSITRONIUM no. 101199807; and the SciMat and qLife Priority Research Areas budget under the program Excellence Initiative - Research University at Jagiellonian University. We also acknowledge the Polish high-performance computing infrastructure PLGrid (HPC Center: ACK Cyfronet AGH) for providing computer facilities and support within computational grant no. PLG/2025/018762 and PLG/2026/020149.

Data Availability Statement: The data supporting the reported results of this study are available upon reasonable request from the authors.

Acknowledgments: This publication is based upon work from COST Action CA24131-ENRICH, supported by the European Cooperation in Science and Technology.

Conflicts of Interest: The authors declare no conflicts of interest.

Abbreviations

The following abbreviations are used in this manuscript:

PET	Positron emission tomography
J-PET	Jagiellonian Positron Emission Tomograph
PLI	Positronium lifetime imaging
PALS	Positron annihilation lifetime spectroscopy
LO	Leading order
TOT	Time over threshold
LOR	Line of response
oPs	Ortho-positronium
pPs	Para-positronium
SSS	Single scatter simulation

References

1. Moskal, P. Positronium imaging. In Proceedings of the 2019 IEEE Nuclear Science Symposium and Medical Imaging Conference (NSS/MIC), Manchester, UK, 26 October–2 November 2019; pp. 1–3. https://doi.org/10.1109/NSS/MIC42101.2019.9059856.
2. Moskal, P.; Bilewicz, A.; Das, M.; Huang, B.; Khreptak, A.; Parzych, S.; Qi, J.; Rominger, A.; Seifert, R.; Sharma, S.; et al. Positronium Imaging: History, Current Status, and Future Perspectives. *IEEE Trans. Radiat. Plasma Med. Sci.* **2025**, *9*, 981–1001. https://doi.org/10.1109/TRPMS.2025.3583554.
3. Moskal, P. Quantum Entanglement Degree, Mean Positronium Lifetime, and the $3\gamma/2\gamma$ Annihilation-Rate Ratio as Novel PET Biomarkers for Hypoxia—Concept, Challenges, and Predictions. *Bio-Algorithms Med-Syst.* **2026**, *22*, 56–77. https://doi.org/10.5604/01.3001.0055.7461.
4. Vandenberghe, S.; Mikhaylova, E.; D'Hoe, E.; Mollet, P.; Karp, J.S. Recent developments in time-of-flight PET. *EJNMMI Phys.* **2016**, *3*, 3. https://doi.org/10.1186/s40658-016-0138-3.
5. Alavi, A.; Werner, T.J.; Stępień, E.Ł.; Moskal, P. Unparalleled and Revolutionary Impact of PET Imaging on Research and Day-to-Day Practice of Medicine. *Bio-Algorithms Med-Syst.* **2021**, *17*, 203–212. https://doi.org/10.1515/bams-2021-0186.
6. Bass, S.D.; Mariazzi, S.; Moskal, P.; Stępień, E. Colloquium: Positronium physics and biomedical applications. *Rev. Mod. Phys.* **2023**, *95*, 021002. https://doi.org/10.1103/RevModPhys.95.021002.
7. Tuomisto, F.; Barthe, M.F.; Čížek, J.; Eijt, S.W.H.; Green, D.G.; Gribakin, G.F.; Hugenschmidt, C.; Kawasuso, A.; Makkonen, I.; Moskal, P.; et al. Positron annihilation spectroscopy. *Nat. Rev. Methods Prim.* **2026**, *6*, 56. https://doi.org/10.1038/s43586-026-00511-5.
8. Jean, Y.C.; Li, Y.; Liu, G.; Chen, H.; Zhang, J.; Gadzia, J.E. Applications of slow positrons to cancer research: Search for selectivity of positron annihilation to skin cancer. *Appl. Surf. Sci.* **2006**, *252*, 3166–3171. https://doi.org/10.1016/j.apsusc.2005.08.101.
9. Chen, H.; Horn, J.D.; Jean, Y.C. Applications of positron annihilation spectroscopy to life science. *Defect Diffus. Forum* **2012**, *331*, 275–293. https://doi.org/10.4028/www.scientific.net/DDF.331.275.

10. Jasińska, B.; Zgardzińska, B.; Chołubek, G.; Gorgol, M.; Wiktor, K.; Wysogld, K.; Białas, P.; Curceanu, C.; Czerwiński, E.; Dulski, K.; et al. Human tissues investigation using PALS technique. *Acta Phys. Pol. B* **2017**, *48*, 1737–1742. https://doi.org/10.5506/APhysPolB.48.1737.
11. Zgardzińska, B.; Chołubek, G.; Jarosz, B.; Wysogląd, K.; Gorgol, M.; Goździuk, M.; Chołubek, M.; Jasińska, B. Studies on healthy and neoplastic tissues using positron annihilation lifetime spectroscopy and focused histopathological imaging. *Sci. Rep.* **2020**, *10*, 11890. https://doi.org/10.1038/s41598-020-68727-3.
12. Moskal, P.; Kubicz, E.; Grudzień, G.; Czerwiński, E.; Dulski, K.; Leszczyński, B.; Niedźwiecki, S.; Stępień, E.Ł. Developing a novel positronium biomarker for cardiac myxoma imaging. *EJNMMI Phys.* **2023**, *10*, 22. https://doi.org/10.1186/s40658-023-00543-w.
13. Moskal, P.; Dulski, K.; Chug, N.; Curceanu, C.; Czerwiński, E.; Dadgar, M.; Gajewski, J.; Gajos, A.; Grudzień, G.; Hiesmayr, B.C.; et al. Positronium imaging with the novel multiphoton PET scanner. *Sci. Adv.* **2021**, *7*, eabh4394. https://doi.org/10.1126/sciadv.abh4394.
14. Moskal, P.; Baran, J.; Bass, S.; Choiński, J.; Chug, N.; Curceanu, C.; Czerwiński, E.; Dadgar, M.; Das, M.; Dulski, K.; et al. Positronium image of the human brain in vivo. *Sci. Adv.* **2024**, *10*, eadp2840. https://doi.org/10.1126/sciadv.adp2840.
15. Moskal, P.; Jasińska, B.; Stępień, E.Ł.; Bass, S.D. Positronium in medicine and biology. *Nat. Rev. Phys.* **2019**, *1*, 527–529. https://doi.org/10.1038/s42254-019-0078-7.
16. Moyo, S.; Stępień, E.; Moskal, P. Characterisation of Plasma Blood Clots in Different Physical States Using Positron Annihilation Lifetime Spectroscopy. *Bio-Algorithms Med-Syst.* **2025**, *21*, 137–145. https://doi.org/10.5604/01.3001.0055.5409.
17. Shibuya, K.; Saito, H.; Nishikido, F.; Takahashi, M.; Yamaya, T. Oxygen sensing ability of positronium atom for tumor hypoxia imaging. *Commun. Phys.* **2020**, *3*, 173. https://doi.org/10.1038/s42005-020-00440-z.
18. Stepanov, P.S.; Selim, F.A.; Stepanov, S.V.; Bokov, A.V.; Ilyukhina, O.V.; Duplâtre, G.; Byakov, V.M. Interaction of positronium with dissolved oxygen in liquids. *Phys. Chem. Chem. Phys.* **2020**, *22*, 5123–5131. https://doi.org/10.1039/C9CP06105C.
19. Moskal, P.; Stępień, E.Ł. Positronium as a biomarker of hypoxia. *Bio-Algorithms Med-Syst.* **2021**, *17*, 311–319. https://doi.org/10.1515/bams-2021-0189.
20. Jasińska, B.; Moskal, P. A New PET Diagnostic Indicator Based on the Ratio of $3\gamma/2\gamma$ Positron Annihilation. *Acta Phys. Pol. B* **2017**, *48*, 1577–1582. https://doi.org/10.5506/APhysPolB.48.1577.
21. Mercolli, L.; Steinberger, W.M.; Läppchen, T.; Amon, M.; Bregenzer, C.; Conti, M.; Cardoso, Â.R.F.; Mingels, C.; Moskal, P.; Rathod, N.; et al. In vivo voxel-wise positronium lifetime imaging of thyroid cancer using clinically routine I–124 PET/CT. *EANM Innov.* **2026**, *2*, 100017. https://doi.org/10.1016/j.eanmi.2025.100017.
22. Huang, B.; Dai, B.; Lapi, S.E.; Liles, G.; Karp, J.S.; Qi, J. High-Resolution Positronium Lifetime Tomography at Clinical Activity Levels on the PennPET Explorer. *J. Nucl. Med.* **2025**, *66*, 1464–1470. https://doi.org/10.2967/jnumed.125.270130.
23. Das, M.; Mryka, W.; Beyene, E.Y.; Parzych, S.; Sharma, S.; Stępień, E.; Moskal, P. Estimating the efficiency and purity for detecting annihilation and prompt photons for positronium imaging with J-PET using toy Monte Carlo simulation. *Bio-Algorithms Med-Syst.* **2023**, *19*, 87–95. https://doi.org/10.5604/01.3001.0054.1938.
24. Moskal, P.; Khreptak, A.; Choiński, J.; Jones, P.; Kadenko, I.; Majkowska-Pilip, A.; Palit, R.; Stolarz, A.; Walczak, R.; Stępień, E. Endorsing Titanium–Scandium Radionuclide Generator for PET and Positronium Imaging. *Acta Phys. Pol. A* **2025**, *148*, S152. https://doi.org/10.12693/APhysPolA.148.S152.
25. Das, M.; Sharma, S.; Beyene, E.Y.; Bilewicz, A.; Choinski, J.; Chug, N.; Curceanu, C.; Czerwinski, E.; Eliyan, K.V.; Hajduga, J.; et al. First positronium imaging using ^{44}Sc with the J-PET scanner: A case study on the NEMA-Image Quality phantom. *IEEE Trans. Radiat. Plasma Med. Sci.* **2026**, *10*, 593–602. https://doi.org/10.1109/TRPMS.2025.3621554.
26. Kubat, K.; Das, M.; Sharma, S.; Beyene, E.Y.; Bilewicz, A.; Choiński, J.; Chug, N.; Curceanu, C.; Czerwiński, E.; Hajduga, J.; et al First ex-vivo positronium imaging of tissues with modular J-PET scanner using ^{44}Sc radionuclide. *Z. Med. Phys.* **2026**, *36*, 357–365. https://doi.org/10.1016/j.zemedi.2026.03.004.
27. Das, M.; Sharma, S.; Beyene, E.Y.; Bilewicz, A.; Choiński, J.; Chug, N.; Curceanu, C.; Czerwiński, E.; Hajduga, J.; Jalali, S.; et al. First positronium lifetime imaging using ^{52}Mn and ^{55}Co with a plastic-scintillator-based PET scanner. *Sci. Rep.* **2026**, *16*, 16230. https://doi.org/10.1038/s41598-026-43965-z.
28. Steinberger, W.M.; Mercolli, L.; Breuer, J.; Sari, H.; Parzych, S.; Niedzwiecki, S.; Lapkiewicz, G.; Moskal, P.; Stepien, E.; Rominger, A.; et al. Positronium lifetime validation measurements using a long-axial field-of-view positron emission tomography scanner. *EJNMMI Phys.* **2024**, *11*, 76. https://doi.org/10.1186/s40658-024-00678-4.
29. Prenosil, G.A.; Sari, H.; Fürstner, M.; Afshar-Oromieh, A.; Shi, K.; Rominger, A.; Hentschel, M. Performance Characteristics of the Biograph Vision Quadra PET/CT System with a Long Axial Field of View Using the NEMA NU 2–2018 Standard. *J. Nucl. Med.* **2022**, *63*, 476–484. https://doi.org/10.2967/jnumed.121.261972.
30. Mercolli, L.; Steinberger, W.M.; Sari, H.; Afshar-Oromieh, A.; Caobelli, F.; Conti, M. In Vivo Positronium Lifetime Measurements with Intravenous Tracer Administration and a Long Axial Field-of-View PET/CT. *IEEE Trans. Radiat. Plasma Med. Sci.* **2026**, *Early Access*. https://doi.org/10.1109/trpms.2026.3687923.

31. Huang, B.; Wang, Z.; Zeng, X.; Goldan, A.H.; Qi, J. Fast high-resolution lifetime image reconstruction for positron lifetime tomography. *Commun. Phys.* **2025**, *8*, 181. https://doi.org/10.1038/s42005-025-02100-6.
32. Dai, B.; Daube-Witherspoon, M.E.; McDonald, S.; Werner, M.E.; Parma, M.J.; Geagan, M.J.; Viswanath, V.; Karp, J.S. Performance evaluation of the PennPET Explorer with expanded axial coverage. *Phys. Med. Biol.* **2023**, *68*, 095007. https://doi.org/10.1088/1361-6560/acc722.
33. Samanta, S.; Sun, X.; Li, H.; Li, Y. Feasibility Study of Positronium Imaging using the NeuroEXPLORER (NX) Brain PET Scanner. In Proceedings of the 2023 IEEE Nuclear Science Symposium, Medical Imaging Conference and International Symposium on Room-Temperature Semiconductor Detectors (NSS MIC RTSD), Vancouver, BC, Canada, 4–11 November 2023; p. 1. https://doi.org/10.1109/NSSMICRTSD49126.2023.10338538.
34. Takyu, S.; Matsumoto, K.; Hirade, T.; Nishikido, F.; Akamatsu, G.; Tashima, H.; Takahashi, M.; Yamaya, T. Quantification of radicals in aqueous solution by positronium lifetime: An experiment using a clinical PET scanner. *Jpn. J. Appl. Phys.* **2024**, *63*, 086003. https://doi.org/10.35848/1347-4065/ad679a.
35. Berens, L.; Hsu, I.; Chen, C.; Halpern, H.; Kao, C.-M. An analytic, moment-based method to estimate orthopositronium lifetimes in positron annihilation lifetime spectroscopy measurements. *Bio-Algorithms Med-Syst.* **2024**, *20*, 40–48. https://doi.org/10.5604/01.3001.0054.9141.
36. Fujimoto, M.; Sato, R.; Hamdan, M.; Uenomachi, M.; Caradonna, P.; Stephenson, L.; Montgomery, A.; Bordes, J.; Brown, J.R.; Watts, D.P.; et al. Advancing PET through direct imaging of three-photon decay using pure positron emitters. *Commun. Phys.* **2026**, *9*, 254. https://doi.org/10.1038/s42005-026-02782-6.
37. Alavi, A.; Revheim, M.E.; Newberg, A.B.; Werner, T.J.; Guedj, E. 18F-Fluorodeoxyglucose PET, the Brain, and Other Organs: From the First Human Studies (1976) to 2026. *PET Clin.* **2026**, *21*, 459–470. https://doi.org/10.1016/j.cpet.2026.05.001.
38. Gurunath Bharathi, P.; Abbaszadeh, S.; Moskal, P.; Alavi, A. Transformative Advances in PET Imaging: From FDG to Total Body Scanners, Novel Tracers and AI-Driven Precision Medicine. *Bio-Algorithms Med-Syst.* **2025**, *21*, 40–57. https://doi.org/10.5604/01.3001.0055.2175.
39. Ore, A.; Powell, J.L. Three-photon annihilation of an electron-positron pair. *Phys. Rev.* **1949**, *75*, 1696–1699. https://doi.org/10.1103/PhysRev.75.1696.
40. Al-Ramadhan, A.H.; Gidley, D.W. New precision measurement of the decay rate of singlet positronium. *Phys. Rev. Lett.* **1994**, *72*, 1632–1635. https://doi.org/10.1103/PhysRevLett.72.1632.
41. Kataoka, Y.; Asai, S.; Kobayashi, T. First test of O(α^2) correction of the orthopositronium decay rate. *Phys. Lett. B* **2009**, *671*, 219–223. https://doi.org/10.1016/j.physletb.2008.12.008.
42. Adkins, G.S.; Cassidy, D.B.; Pérez-Ríos, J. Precision spectroscopy of positronium: Testing bound-state QED theory and the search for physics beyond the Standard Model. *Phys. Rep.* **2022**, *975*, 1–61. https://doi.org/10.1016/j.physrep.2022.05.002.
43. Tao, S.J. Positronium annihilation in molecular substances. *J. Chem. Phys.* **1972**, *56*, 5499–5510. https://doi.org/10.1063/1.1677067.
44. Eldrup, M.M.; Lightbody, D.; Sherwood, J.N. The temperature dependence of positron lifetimes in solid pivalic acid. *Chem. Phys.* **1981**, *63*, 51–58. https://doi.org/10.1016/0301-0104(81)80307-2.
45. Das, M.; Bayerlein, R.; Sharma, S.; Parzych, S.; Niedźwiecki, S.; Badawi, R.; Beyene, E.Y.; Chug, N.; Curceanu, C.; Czerwiński, E.; et al. Development of correction techniques for the J-PET scanner. *Bio-Algorithms Med-Syst.* **2024**, *20*, 101–110. https://doi.org/10.5604/01.3001.0054.9362.
46. Kasperska, K.; Skurzok, M.; Moskal, P. Studies of Attenuation Effects in Two- and Three-Photon Positronium Decays in Phantom Models. *Bio-Algorithms Med-Syst.* **2025**, *21*, 42–51. https://doi.org/10.5604/01.3001.0055.5414.
47. Skurzok, M.; Bass, S.D.; Kasperska, K.; Beyene, E.; Chug, N.; Curceanu, C.; Czerwiński, E.; Das, M.; Gorgol, M.; Jalali, S.; et al. Experimental determination of the Dalitz plot for positronium decay using the J-PET detection system. *Phys. Lett. B* **2026**, *882*, 141018. https://doi.org/10.1016/j.physletb.2026.141018.
48. Moskal, P.; Gajos, A.; Mohammed, M.; Chhokar, J.; Chug, N.; Curceanu, C.; Czerwiński, E.; Dadgar, M.; Dulski, K.; Gorgol, M.; et al. Testing CPT symmetry in ortho-positronium decays with positronium annihilation tomography. *Nat. Commun.* **2021**, *12*, 5658. https://doi.org/10.1038/s41467-021-25905-9.
49. Gajos, A.; Kamińska, D.; Czerwiński, E.; Alfs, D.; Bednarski, T.; Białas, P.; Głowacz, B.; Gorgol, M.; Jasińska, B.; Kapłon, Ł.; et al. Trilateration-based reconstruction of ortho-positronium decays into three photons with the J-PET detector. *Nucl. Instrum. Methods Phys. Res. A* **2016**, *819*, 54–59. https://doi.org/10.1016/j.nima.2016.02.069.
50. Chug, N.; Bass, S.D.; Beyene, E.Y.; Curceanu, C.; Czerwiński, E.; Das, M.; Eliyan, K.V.; Gorgol, M.; Hajduga, J.; Jalali, S.; et al. Studies of CPT symmetry in positronium decays with the 192 plastic strip J-PET detector. *Phys. Rev. D* **2026**, *113*, 032003. https://doi.org/10.1103/wy7r-xgl9.
51. Abuelhia, E.; Kacperski, K.; Spyrou, N.M. Three-photon annihilation in PET: 2D imaging experiments. *J. Radioanal. Nucl. Chem.* **2007**, *271*, 489–495. https://doi.org/10.1007/s10967-007-0235-9.
52. Eldrup, M.M.; Mogensen, O.; Trumpy, G. Positron Lifetimes in Pure and Doped Ice and in Water. *J. Chem. Phys.* **1972**, *57*, 495–504. https://doi.org/10.1063/1.1677990.

53. Dulski, K.; Beyene, E.; Chug, N.; Curceanu, C.; Czerwiński, E.; Das, M.; Gorgol, M.; Jasińska, B.; Kacprzak, K.; Kapłon, Ł.; et al. Nanoporosity imaging by positronium lifetime tomography. *Nucl. Instrum. Methods Phys. Res. A* **2026**, *1086*, 171311. https://doi.org/10.1016/j.nima.2026.171311.
54. Sharma, S.; Baran, J.; Chug, N.; Baran, J.; Chug, N.; Curceanu, C.; Czerwiński, E.; Dadgar, M.; Dulski, K.; Eliyan, K.; et al. Efficiency determination of J-PET: First plastic scintillators-based PET scanner. *EJNMMI Phys.* **2023**, *10*, 28. https://doi.org/10.1186/s40658-023-00546-7.
55. Kamińska, D.; Gajos, A.; Czerwiński, E.; Alfs, D.; Bednarski, T.; Białas, P.; Curceanu, C.; Dulski, K.; Głowacz, B.; Gupta-Sharma, N.; et al. A feasibility study of ortho-positronium decays measurement with the J-PET scanner based on plastic scintillators. *Eur. Phys. J. C* **2016**, *76*, 445. https://doi.org/10.1140/epjc/s10052-016-4294-3.
56. Carney, J.P.J.; Townsend, D.W.; Rappoport, V.; Bendriem, B. Method for transforming CT images for attenuation correction in PET/CT imaging. *Med. Phys.* **2006**, *33*, 976–983. https://doi.org/10.1118/1.2174132.
57. Kinahan, P.E.; Hasegawa, B.H.; Beyer, T. X-ray-based attenuation correction for positron emission tomography/computed tomography scanners. *Semin. Nucl. Med.* **2003**, *33*, 166–179. https://doi.org/10.1053/snuc.2003.127307.
58. Bayerlein, R.; Das, M.; Sharma, S.; Badawi, R.D.; Beyene, E.Y.; Chug, N.; Curceanu, C.; Czerwiński, E.; Eliyan, K.V.; Hajduga, J.; et al. Monte Carlo-based scatter correction for the plastic-based modular PET scanner J-PET. *Phys. Med. Biol.* **2026**, *71*, 075026. https://doi.org/10.1088/1361-6560/ae54fb.
59. Watson, C.C. New, faster, image-based scatter correction for 3D PET. *IEEE Trans. Nucl. Sci.* **2000**, *47*, 1587–1594. https://doi.org/10.1109/23.873020.
60. Accorsi, R.; Adam, L.-E.; Werner, M.E.; Karp, J.S. Optimization of a fully 3D single scatter simulation algorithm for 3D PET. *Phys. Med. Biol.* **2004**, *49*, 2577–2598. https://doi.org/10.1088/0031-9155/49/12/008.
61. Niekämper, D.; Scheins, J.J.; Pfaehler, E.; Herraiz, J.L.; Shah, N.J.; Lerche, C. Improved random coincidence estimation including triple coincidence detection in PET. *Front. Nucl. Med.* **2026**, *6*, 1739575. https://doi.org/10.3389/fnume.2026.1739575.
62. Brasse, D.; Kinahan, P.E.; Lartizien, C.; Comtat, C.; Casey, M.; Michel, C. Correction methods for random coincidences in fully 3D whole-body PET: Impact on data and image quality. *J. Nucl. Med.* **2005**, *46*, 859–867.
63. Sane, P.; Salonen, E.; Falck, E.; Repakova, J.; Tuomisto, F.; Holopainen, J.M.; Vattulainen, I. Probing biomembranes with positrons. *J. Phys. Chem. B* **2009**, *113*, 1810–1812. https://doi.org/10.1021/jp809308j.
64. Sane, P.; Tuomisto, F.; Holopainen, J.M. Void volume variations in contact lens polymers. *Contact Lens Anterior Eye* **2011**, *34*, 2–6. https://doi.org/10.1016/j.clae.2010.06.008.
65. Pamuła, E.; Dryzek, E. Structural Changes in Surface-Modified Polymers for Medical Applications. *Acta Phys. Pol. A* **2008**, *113*, 1485–1493.
66. Kilburn, D.; Townrow, S.; Meunier, V.; Richardson, R.; Alam, A.; Ubbink, J. Organization and mobility of water in amorphous and crystalline trehalose. *Nat. Mater.* **2006**, *5*, 632. https://doi.org/10.1038/nmat1681.
67. Swartz, H.M.; Flood, A.B.; Schaner, P.E.; Halpern, H.; Williams, B.B.; Pogue, B.W.; Gallez, B.; Vaupel, P. How best to interpret measures of levels of oxygen in tissues to make them effective clinical tools for care of patients with cancer and other oxygen-dependent pathologies. *Physiol. Rep.* **2020**, *8*, e14541. https://doi.org/10.14814/phy2.14541.
68. Vaupel, P.; Flood, A.B.; Swartz, H. M Oxygenation Status of Malignant Tumors vs. Normal Tissues: Critical Evaluation and Updated Data Source Based on Direct Measurements with p_O2 Microsensors. *Appl. Magn. Reson.* **2021**, *52*, 1451–1479. https://doi.org/10.1007/s00723-021-01383-6.
69. Nasiri, R.; Sankaranthi, A.; Pratx, G. Organ-on-a-chip systems for modeling tumor and normal tissue microenvironments in radiotherapy research. *Trends Biotechnol.* **2026**, *44*, 333–350. https://doi.org/10.1016/j.tibtech.2025.07.002.
70. McKeown, S.R. Defining normoxia, physoxia and hypoxia in tumours-implications for treatment response. *Br. J. Radiol.* **2014**, *87*, 20130676. https://doi.org/10.1259/bjr.20130676.

Disclaimer/Publisher's Note: The statements, opinions and data contained in all publications are solely those of the individual author(s) and contributor(s) and not of MDPI and/or the editor(s). MDPI and/or the editor(s) disclaim responsibility for any injury to people or property resulting from any ideas, methods, instructions or products referred to in the content.